Numerical Investigation of the Aerodynamic and Aero acoustic Interactions Between a Tractor Propeller and a Lifting Wing

Barker, Jack E.; Zarri, Alessandro; Christophe, Julien; Schram, Christophe

DOI
10.2514/6.2023-4056

Publication date
2023

Document Version
Final published version

Published in
AIAA Aviation and Aeronautics Forum and Exposition, AIAA AVIATION Forum 2023

AIAA AVIATION Forum
12-16 June 2023, San Diego, CA and Online
AIAA AVIATION 2023 Forum

10.2514/6.2023-4056

Numerical Investigation of the Aerodynamic and Aeroacoustic Interactions Between a Tractor Propeller and a Lifting Wing

Jack E. Barker*†, Alessandro Zarri‡, Julien Christophe§, and Christophe Schram¶
von Karman Institute for Fluid Dynamics, 1640 Rhode-St-Genèse, Belgium

The Urban Air Mobility market is currently experiencing rapid growth with significant investments directed toward the development of novel aircraft designs aimed at enhancing performance efficiency and reducing climate impact. Nevertheless, the emergence of noise pollution as a result of aircraft flying closer to previously undisturbed populations is now a pressing concern. Tonal noise, in particular, is widely recognized as the most prevalent and disruptive form of noise pollution. This study proposes a hybrid computational methodology that prioritizes the evaluation of installation effects on a single tractor propeller and wing case, with a specific focus on tonal noise. The hybrid methodology consists of simulating the near-field aerodynamics over the different geometries using an unsteady Reynolds-Averaged Navier-Stokes commercial solver to determine the equivalent sources. Then, the calculation of the acoustic scattering and propagation is handled by a commercial numerical acoustic solver based on the Finite Element Method. This low-order methodology allows discriminating between aerodynamic and acoustic installation effects with moderate computational times. The directivity results indicate that both aerodynamic and acoustic installation effects cause moderate changes in sound level. However, the aerodynamic installation has a greater impact on the directivity, particularly above and below the wing. The noise generated by the unsteady flow over the wing in the propeller-wing geometry is comparable to the levels of propeller noise. However, it radiates in directivity additional to that of the blades, thereby changing the overall directivity and sound level significantly.

I. Introduction

The Urban Air Mobility (UAM) market is new and rapidly growing with approximately $5.5 billion invested in their development as of 2021, which is forecasted to exceed $32 billion worldwide by 2035 for intercity UAM services, with the overall market scope reaching up to $320 billion [1]. Here novel aircraft designs are being investigated with the goal of increased performative efficiency and reduced overall climate impact. These concepts include a range of designs such as leading-edge distributed electric propulsion (DEP) [2], over-the-wing electric propulsion [3], tip-mounted electric propulsion [2], contra-rotating propellers[4], shrouded propellers [5], and combinations of these.

While many of these designs appear promising, the noise generation of the systems must also be addressed, since such concepts are often built to fly lower and closer to communities that were previously undisturbed by air traffic noise [6, 7]. These vehicles may be disturbing to both humans [8] as well as animals and their habitats [9].

This study primarily examines DEP in tractor (also called puller) configurations for forward-flight applications, examining how the addition of a wing affects an individual propeller's performance and noise-generating mechanisms. Propellers are known to create tonal noise at frequency peaks that correspond to the Blade Passage Frequency (BPF) and its harmonics [10, 11], as well as broadband noise from the motion of the propeller and random force fluctuations associated with turbulence.

The Ffowcs-Williams and Hawkings analogy (FW-H) describes flow-induced sound generation using quadrupolar, dipolar, and monopolar equivalent sources, corresponding to different mechanisms [12]. Considering the propeller first, at low subsonic tip Mach numbers and for an acoustically compact blade chord, two mechanisms are found to be most relevant: thickness noise and loading noise. Thickness noise is a result of the displacement of the air by the volume of

*Short Training Program student, Environmental and Applied Fluid Dynamics dept, 72 chaussée de Waterloo, Belgium.
†MSc Student, Delft University of Technology, Faculty of Aerospace Engineering, Kluyverweg 1, 2629HS, Delft, The Netherlands.
‡Post-doctoral researcher, Environmental and Applied Fluid Dynamics dept, 72 chaussée de Waterloo, Belgium.
§Senior research engineer, Environmental and Applied Fluid Dynamics dept, 72 chaussée de Waterloo, Belgium.
¶Professor, Environmental and Applied Fluid Dynamics & Aeronautics and Aerospace depts, 72 chaussée de Waterloo, Belgium, AIAA Senior Member.

the propeller and is modeled as a monopolar term. Loading noise is related to the forces on the blades and is modeled as a dipolar term [11]. Those forces can be steady when the propeller rotates in an azimuthally-homogeneous flow field (steady-loading noise), or unsteady. In the second case, the unsteadiness can result from the ingestion of a wake or boundary layer for example, or be caused by a nearby downstream element inducing a potential distortion of the flow traversed by the blades. Besides the noise produced by the propeller, the impingement of its wakes on the wing causes lift fluctuations of the latter, which also radiate unsteady loading noise. Those mutual interactions between the propeller and airframe are called *aerodynamic installation effects* [10].

Both mechanisms are periodic, so the main contribution to loudness is constituted by harmonic tones, viewed as one of the most bothersome components of the emitted spectrum [13]; because of this, this study will concentrate on tonal noise and neglect broadband noise. Furthermore, the propeller model used in this project has a small thickness-to-chord ratio, so thickness noise is not the focus of this paper.

In addition to the aerodynamic effects, the scattering of the propeller noise by the wing can significantly change the directivity and cause either shielding or amplification effects in both the near- and far-field. These *acoustic installation effects* [14] will also be investigated in this paper.

A similar wing-propeller problem was studied, experimentally and numerically, by Zawodny *et al.* [15]. In their study acoustic predictions showed equivalent contributions from the propeller and wing loading noise sources, and suggested that both aerodynamic and acoustic installation effects need to be considered when analyzing a propeller-wing geometry. They also used a stationary monopole and simplified geometry to determine the scattering effects which, as noted in the paper, does not fully model the case and led to results that do not fully agree.

The objective of this work is to determine the relative importance of the aerodynamic and acoustic installation effects on a single tractor propeller-wing case. A hybrid computational methodology is proposed to this end, in which an unsteady Reynolds-Averaged Navier-Stokes (uRANS) commercial solver is used to determine the equivalent sources, and the calculation of the acoustic scattering is handled by a commercial numerical acoustic solver based on the Finite Element Method (FEM). This low-order methodology allows discriminating between aerodynamic and acoustic installation effects with quite moderate computational times.

II. Methodology

The TUD-XPROP-S model, featuring six blades and a spinner, is depicted in black in Figure 1. The propeller has a radius of 0.1016 m and a pitch of 30° at 70% span. Every simulation is run using a rotation speed of 8858.2 RPM, giving an advance ratio of $J = 1$ with a freestream speed of 30 m/s and a blade tip Mach number of 0.29. This also corresponds with a Reynolds number of 4.45×10^4 at the tip with a chord of 6.8 mm. In what follows, the BPFs will be found at frequencies equal to $6nf_{rev}$, with $n = 1, 2, \ldots$ and $f_{rev} = 147.64$ Hz.

For the case of the isolated propeller, an arbitrary nacelle was designed to approximate the housing and support from the wind tunnel test. The validation results from the wind tunnel are based on a force sensor detecting thrust from only the spinner-blade assembly, therefore the particular form of the nacelle should have little influence [16]. In the propeller-wing case (see Figure 1), the geometry based on the wind-tunnel experiments carried out in Ref. [17] was also provided by TU Delft; however, the wing tips were extended to reduce tip effects on the solution as the wind tunnel geometry is not simulated. In this model, an NLF-MOD22(B) airfoil [18] is mounted at $\approx 5°$ to the freestream flow and thrust direction with the propeller plane 0.85 diameters ahead. This distance is a typical distance for a propeller-wing geometry and the one used in the experimental campaign.

A. uRANS Flow Simulations

To model the flow around the propeller, the commercial software Simcenter STAR-CCM+ Version 17.02 is used [19]. This solves the unsteady Reynolds Averaged Navier-Stokes (uRANS) equations with Menter's Shear Stress Transport turbulence model [20]. A compressible flow solution is used to accurately predict the flow characteristics at the given tip Mach number.

The simulation is initialized using a steady RANS solution employing a three-dimensional coupled implicit scheme for a moving reference frame (MRF) approach around the propeller region. This approach is similar to the one used in [21]. For the uRANS simulations, a second-order temporal discretization is used with a time step of 1.881×10^{-5} s, which corresponds to 1° of rotation. The same MRF region is used to create a sliding mesh for the uRANS simulations, and its width is set to $1.25D$, where D is the propeller diameter. This width is selected to ensure a uniform mesh size at the interface of the sliding region and the rest of the mesh at every angle of rotation of the blade, similarly following Ref. [22]. In addition, with the time step of 1° at the furthest diameter, the displacement of a cell is not more than the

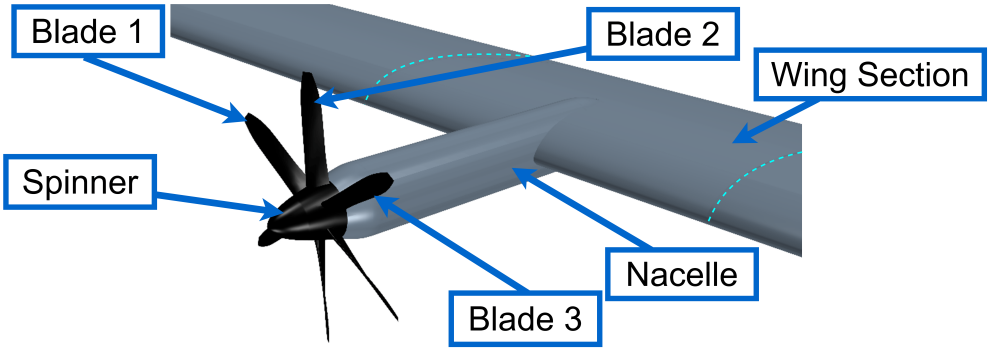

Fig. 1 Full wing geometry with nomenclature.

length of the cell next to it in the non-rotating domain. This ensures continuity across the interface creating lower errors at the transition from rotating to steady regions.

Moreover, this width is used as a sizing parameter, such that $L = 1.25D$, and determines the rest of the domain size. The domain is a bullet-shaped domain with a radius of $12.5L$ for the spherical inlet, which causes the cylinder to have the same radius. The diameter extends $25L$ downstream. This domain size is selected to ensure that the boundaries do not influence the local solution.

The boundary conditions are set as follows: the inlet is a velocity inlet with a $30\,\mathrm{m\,s^{-1}}$ component in the axial direction, the sides are a boundary-normal freestream, and the exit is a pressure outlet. These boundary conditions provide uniformity between simulations by allowing the domain to be utilized for all models examined, including potential future distributed propulsion simulations. The boundary conditions are shown in Figure 2(a).

The cell count for this study is purposefully kept as low as possible resulting in a mesh size for the isolated propeller of approximately 12.5×10^6 cells and 20×10^6 cells for the propeller-wing configuration. The mesh is tailored to increase cell count in critical areas such as blade roots and tips, however, it was also found that refining the path of the tip vortices is crucial for retaining flow information downstream to the wing. As a result, both the isolated propeller and propeller-wing cases were solved using the hollow cylinder depicted in Figure 2(b).

In order to meet the solver requirements, a prism layer consisting of 15 layers with a thickness of approximately 0.5 mm was applied to all surfaces near the blade. The number of layers was reduced to 5 on the extended area of the wing to decrease the cell count and computational time. This allowed for a $y^+ < 1$ for most of the blade, nacelle, and wing section of interest. The uRANS simulations used 10 sub-iterations per time step, resulting in a continuity residual of below 10^{-6} in both the isolated propeller and propeller-wing cases. The radial momentum residuals were below 10^{-3}, and the axial momentum was below 10^{-5}. Additionally, the turbulent kinetic energy in the isolated case was resolved to a value of 5×10^{-8}, whereas in the propeller-wing case, it was resolved to 10^{-6}. All residuals are non-normalized values.

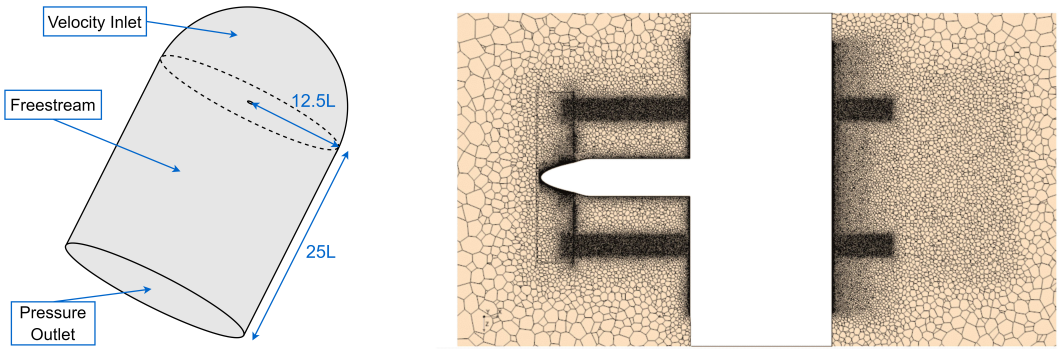

Fig. 2 (a) A diagram of the total domain used for all aerodynamic simulations and the corresponding boundary conditions for each surface. (b) Mesh cut plane depicting the refinement section, the sliding mesh boundary, and the extra hollow-cylinder refinement.

B. FEM Acoustic Simulations

The tonal noise emissions for this study are calculated using a commercial Finite Element Method (FEM) solver, Simcenter 3D [23]. The surfaces of the geometric models are discretized with linear triangular elements of 3 mm in order to accurately describe the geometry, which can still be complex despite neglecting the blades (represented in the model as equivalent sources). In the cases in which the wing is present parts of the wing's upper and lower surface are coarsened to 8 mm to help lower the computational load.

The FEM domain exterior surface boundary condition is a non-reflective surface with an Automatically Matched Layer coupled with a Kirchoff radiation surface [24]. This allows for the acoustic solution to be propagated to listener locations outside the computational domain. Between these two boundaries, tetrahedral elements are used to fill the volume. The elements in this mesh are chosen such that they generally follow the rule-of-thumb that considers about 6 elements per wavelength of the frequency of interest, however, thanks to the use of the Adaptive Order FEM solver employed in the software, which refines the mesh as needed for each frequency analysis, this sizing is less constrictive [23].

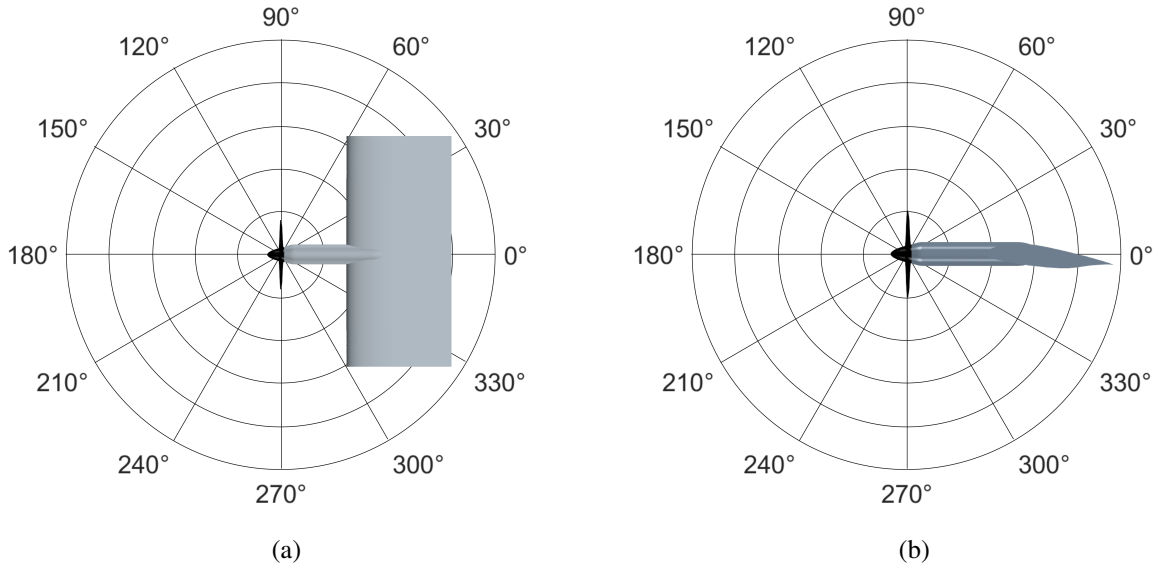

Fig. 3 Directivity definition for the acoustic results in the (a) horizontal plane (top-down view), and (b) in the vertical plane.

The CFD solver allows the output of CFD General Notation System (CGNS) files which can be used to describe the pressure over the surfaces in the simulation. These files are then used as inputs for the acoustic solver. For this study, two sets of data were exported: *i*) from the isolated propeller case the pressure on the six blades (not including the spinner or nacelle) was taken, *ii*) in the propeller-wing case the pressure on the six blades and the pressure over the section of the wing immediately behind the propeller were taken as separate files for the same physical time step (again, neither including the spinner nor nacelle).

For the data from the blades, which are rotating sources, fixed dipole sources are calculated in an analogous reconstruction of rotating dipolar sources; this is known as the *source-mode* method [25]. The dipole source strengths are obtained by integrating the transient pressure field over 5 acoustically-compact segments per blade. The three components of the force per segment are calculated and in the frequency domain reconstructed from the rotating source to stationary components. These source modes are then projected on the high-order degrees of freedom of the finite element problem.

For the pressure data over the wing section, the sources are modeled as surface dipoles. In simulations that include the wing as a source, it is represented as solely a distribution of equivalent dipoles, thereby removing the wing from the acoustic model as a scattering entity, assuming that the dipoles account for the scattering. This implies that the acoustic pressure fluctuations radiated by the propeller and wing were able to propagate from the blades to the other surfaces in the compressible CFD simulation. Under this condition, the pressure data from the wing surface already includes the pressure fluctuations due to the acoustic pressures. For more details on both source types see Ref. [23].

Typical CFD second-order schemes require around 18-25 nodes per wavelength to properly refine the propagation

of the acoustic pressure [26]. In the CFD simulations of this study, the refined region of the hollow cylinder has the fidelity to propagate acoustic pressure up to frequencies corresponding with the 14^{th} BPF but, in the coarse region only wavelengths up to the 3^{rd} BPF can be considered using this criterion conservatively (the 4^{th} BPF falls near the minimum). Additionally, it should be noted that this particular criterion has been established solely for use with homogeneous meshes, rather than accounting for the discontinuity resulting from the implementation of the hollow cylinder method. As a result, the current analysis will concentrate solely on the first and second BPFs, as these frequencies are more resistant to this issue.

III. Results

A. Validation of Aerodynamic Methodology

The use of a hollow cylinder refinement in the aerodynamic simulation allowed the propagation of the flow effects of the blades downstream to interact with the wing. As visualized in Figure 5 the tip vortices from each individual propeller, represented by the $\lambda 2$ criterion, propagate sufficiently far downstream to detail the interaction with the wing. This shows that information can travel both downstream and upstream at locations of interest in the simulation.

The performance characteristics obtained from the simulation show that the isolated propeller simulation was sufficiently accurate. Experimental data at an advance ratio of $J = 1$ and an inlet velocity of $30\,\mathrm{m\,s^{-1}}$ for the isolated propeller from TU Delft resulted in a temporally averaged thrust coefficient of $T_c = 0.45 \pm 0.005$ for the blades and spinner where $T_c = T/(1/2\rho_0 v_0^2 \pi R^2)$ [16]. The simulation gives a value of $T_c = 0.477$ at the same conditions which is within 6% of the experimental results. A mesh refinement study on the simulation also showed less than a 0.1% change in thrust between 12.5 million and 22 million mesh sizes (Figure 4(a)).

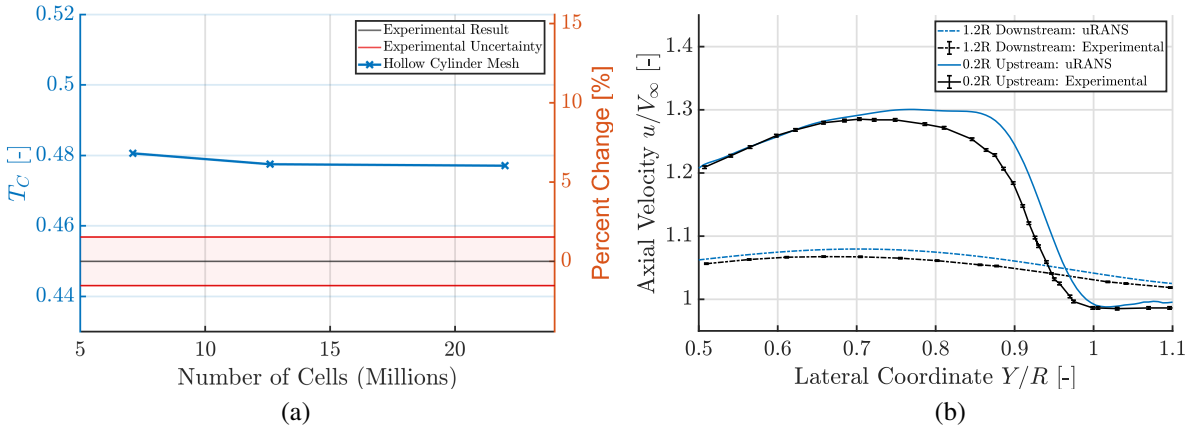

Fig. 4 (a) Mesh convergence study of the blade thrust for the isolated propeller case. (b) Axial velocity profiles upstream and downstream of the propeller compared with experimental data [16].

In order to further validate the accuracy of the aerodynamic simulation, axial velocity profiles were measured upstream and downstream of the propeller and compared with the experimental data from TU Delft. At the same advance ratio and inlet velocity previously compared the simulation showed a maximum difference of 1.25% from the experimental data at 0.2 radii upstream of the propeller, and 4.25% at 1.2 radii downstream. The general trend of the axial velocity profiles is well captured for the isolated propeller case as shown in Figure 4(b). These results demonstrate how well the simulation captured the propeller's flow characteristics and suggest that it is able to appropriately detail the propeller's interaction with the wing.

B. Aerodynamic Effects of the Wing

The aerodynamic installation effects of the wing cause the flow characteristics to alter in the area of the propeller-wing interaction. The flow behind the propeller in the presence of the wing, as visualized in Figure 5(a), does not follow the path that is anticipated for an isolated propeller. This change in wake direction and shape is detailed in Figure 5(b) which compares the simulation results with and without the wing. In the lateral direction, the wing appears to shift the

vortices in the direction of rotation. This is due to the up-going blade creating an increased angle of attack over the wing and lower pressure over the upper surface while the down-going blade performs the opposite effect.

There is also an influence on the potential flow from the wing which curves the streamlines, and thus the blade tip vortices around it. The effect can be seen upstream but appears to be minimal at the distance of the propeller's plane of rotation. This change in the flow field alters the inflow conditions experienced by the propellers increasing the thrust of the blades by 3.5%. While this change is small, this variation alone will change the overall noise. The distortion of the flow also causes a shift in the mean force direction which creates low-order azimuthal distortion.

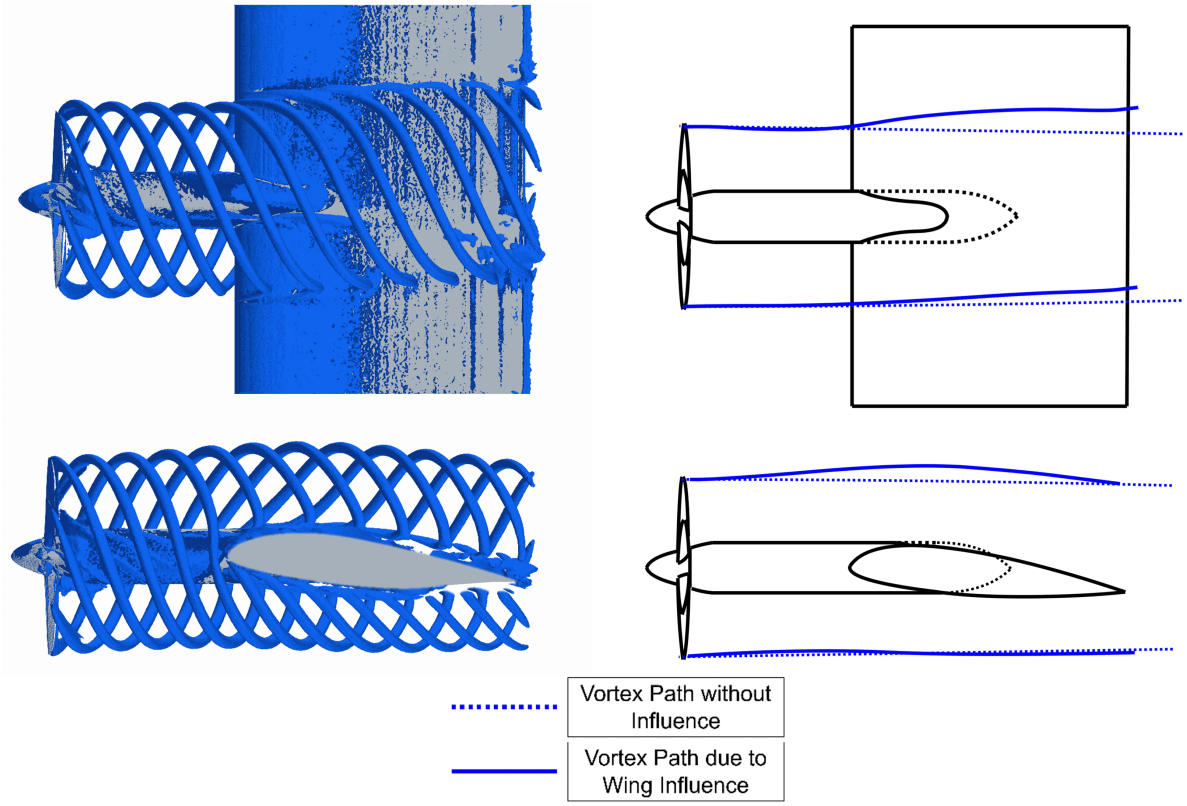

Fig. 5 (a) The vorticity magnitude on the λ_2 criterion for $\lambda_2 = -1.5 \times 10^5$ $1/s^2$ of propeller-wing case. (b) Diagram of the path difference between the isolated propeller case and the propeller-wing case.

C. Verification and Comparison of Acoustic Methodologies

For the case of the isolated propeller, it is expected that the directivity results would only vary with the listener angle relative to the axis due to axial symmetry. This is indeed observed in Figure 6(a) for the main radiation directions, with some deviations for directivities near the axis where the amplitudes are much weaker. This is due to the resolution limitations of the CFD solution. Small or negligible fluctuations of pressure are not fully resolved in the thrust direction leading to inconsistent results possibly dominated by numerical noise in different listener planes. From this, only results at the harmonics and generally near the plane of rotation are analyzed for the isolated propeller.

In Figure 6(b) the results of the isolated propeller acoustic simulation using the uRANS-FEM hybrid methodology are compared with the solution to the Ffowcs-Williams and Hawking acoustic analogy using the Farassat 1A formulation that is included in the commercial CFD solver [19, 27]. In this solid surface FW-H model, the sources include both the loading and thickness noise. The results between the two methodologies closely agree for the loading noise, verifying the applicability of the hybrid methodology approach for predicting the acoustic signature of isolated propellers in the far-field field near the plane of rotation for the propeller. This plot also indicates that loading noise is dominant over the thickness noise along the principal radiation angles.

Additionally, the shape of the directivity indicates a strong influence from the tangential component of the force. If the force were solely fluctuating in the axial direction, there would be no noise in the plane of rotation. In this case, the magnitude of tangential force oscillations is found to be almost half the value of thrust amplitude at the first harmonic.

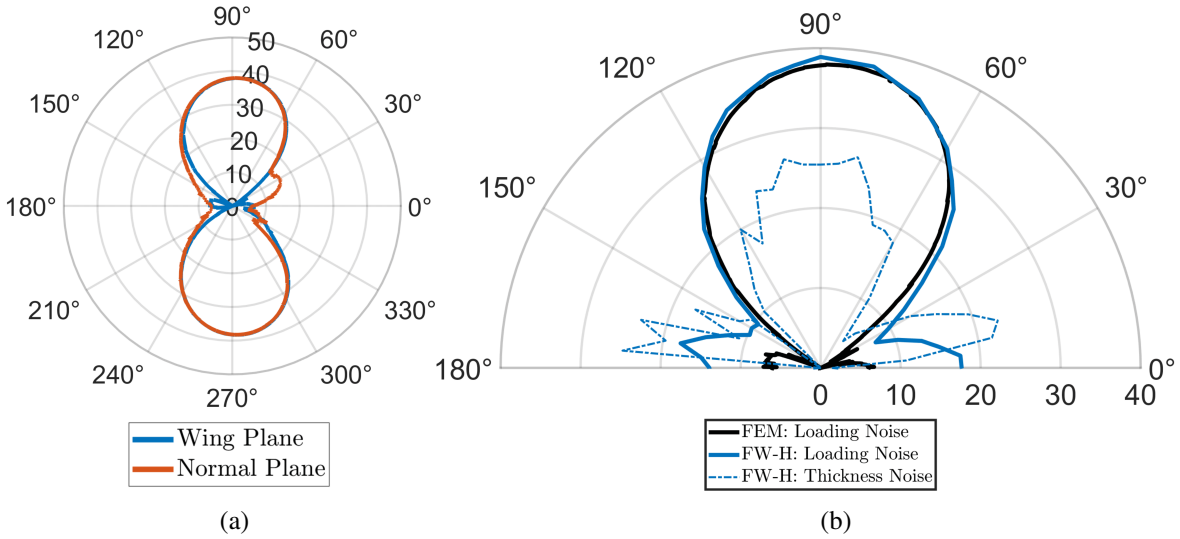

Fig. 6 (a) Directivity at the 1^{st} BPF in perpendicular planes around the isolated propeller. (b) Noise components at the 1^{st} BPF of the isolated propeller comparing the solid surface FW-H solution and the FEM-Source Mode method solution.

D. Aerodynamic Installation Effects on Blade Noise

The thrust BLHs on the reference propeller blade are shown in Figure 7(a) for the free propeller, and in Figure 7(b) in the presence of the wing. Each graph in Figure 7 shows the BLHs calculated over three successive revolutions of the CFD run, in order to highlight the periodic behavior of the calculated forces. It shows fairly low levels for the fluctuations, at least 4 orders of magnitude smaller than the mean component. Given these low values of the BLHs, their interpretation should be conducted with care, especially for the highest harmonics that would correspond to large azimuthal orders of the distortion, hardly justifiable on physical grounds and that could be more related to numerical artifacts.

The potential distortion introduced by the wing at the level of the propeller is expected to show relatively low azimuthal orders, corresponding to the mean flow deflection associated with the lift of the wing and to the deflection of the streamlines approaching its leading edge. Comparing the thrust BLHs without the wing (Figure 7(a)) and with the wing (Figure 7(b)) shows that the first BLHs are indeed substantially increased in the presence of the wing, gaining 3 to 4 orders of magnitude for the first three BLHs. But higher harmonics, up to the 16th or so, seem also affected by the presence of the wing. Those differences should however be interpreted with care, as the absolute values of those BLHs remain fairly low and potentially subject to numerical inaccuracies, even if they remain constant for the three successive revolutions presented here. The higher BLHs and the steady loading are only marginally affected by the presence of the wing.

Considering now the noise radiation (Figure 8(a)), at the 1^{st} BPF changes in the sound level are relatively balanced in the rotor plane, with an increase of 2.01 dB in the blade down direction (between $90°\pm15°$ in the horizontal plane) and a decrease of 3.92 dB (between $270°\pm15°$ in the horizontal plane). Additionally, there is an increase of 6.94 dB below the propeller and a decrease of about 6.83 dB above it. These results indicate that the aerodynamic installation primarily affects directivity.

It is interesting to note that the introduction of the wing's aerodynamic effects results in more sound below the wing than for the free propeller. This finding is significant in the context of Urban Air Mobility (UAM) applications, where this type of geometry will fly overhead of the typical listener.

The wing's presence has a noticeable impact on the noise generated, even when the leading edge is 0.85 diameters downstream, as in this case. This effect is due to the induced velocity upstream of the wing, which causes the upper

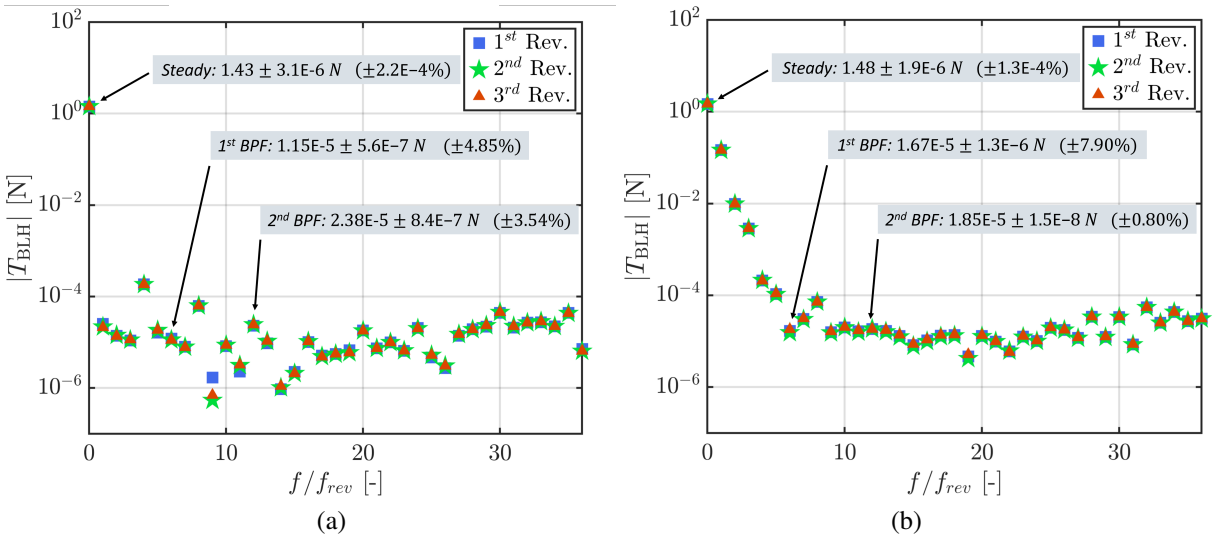

Fig. 7 (a) Thrust BLHs of a single propeller for the isolated propeller. (b) Thrust BLHs of a single propeller in the presence of the wing.

portion of the blade to experience higher velocity and the lower part to experience lower velocity relative to each other. Despite this asymmetry, the maximum change in inflow velocity is only 4.7%, which explains the small change in loading. However, these velocity differences cause the blade to experience varying angles of attack throughout its rotation, resulting in changes in loading during a blade's revolution. As a result, the periodicity of the sound produced increases, leading to the observed BLH increases.

The directivity of the second BPF is more significantly affected by the presence of the wing than the first one. This is justified by the increase of the BLHs with frequencies close to $f/f_{rev} = 12$ that was observed in Figure 7. It should however be reminded that even in presence of the wing, the magnitudes of those BLHs being 5 orders of magnitude below the steady loading, their accuracy might remain questionable given the low-order discretization schemes of the CFD solver. The aerodynamic installation effects on the second BPF would need to be verified using higher-order schemes.

E. Acoustic Installation Effects on Blade Noise

The installation of a wing behind the propeller introduces a solid body into the aerodynamic domain that will scatter waves generated by the rotating blades. This phenomenon is of particular relevance, given that the chord length of the wing is 30 cm, while the wavelength of the first BPF is approximately 38.4 cm. The wing is therefore not compact along its chordwise direction. Furthermore, the wing is situated in the near-field of the blade sources, and previous research has demonstrated that the scattering of the acoustic near-field can substantially affect the far-field directivity as well, irrespective of the compactness of the scattering body [28]. A comparison of cases with and without acoustic installation effects is presented in Figure 8(b), highlighting the impact of this phenomenon.

Regarding the horizontal plane, effectively the plane of the wing despite the angle of attack, the directivity exhibits minimal changes at the dominant lobes. The minor amplification observed originates from scattering sources on the wing, which radiate outward. Two small jumps at approximately 30° and 340° result from thrust noise scattered off the wing's surface. The absence of sources from the spinner, combined with the shielding effect of the wing and nacelle, results in the gap between these two jumps. Finally, the bump in the forward directivity is attributable to direct scattering off the wing's leading edge and the nacelle.

Much like the horizontal plane, the sound level increases in almost all directivities in the vertical plane. The only directivity in which the noise is decreased is at an angle of 10° in which the shielding of the wing reduces the sound. The increased levels between 120° and 210° are due to the scattering of the leading edge. In general, it appears that the effects of acoustic installation are slightly smaller than that of aerodynamic installation with a maximum increase of 6.11 dB in the rotor plane above the wing and 3.13 dB in the rotor plane below it. The average change in the lobes in both planes is only 3.12 dB.

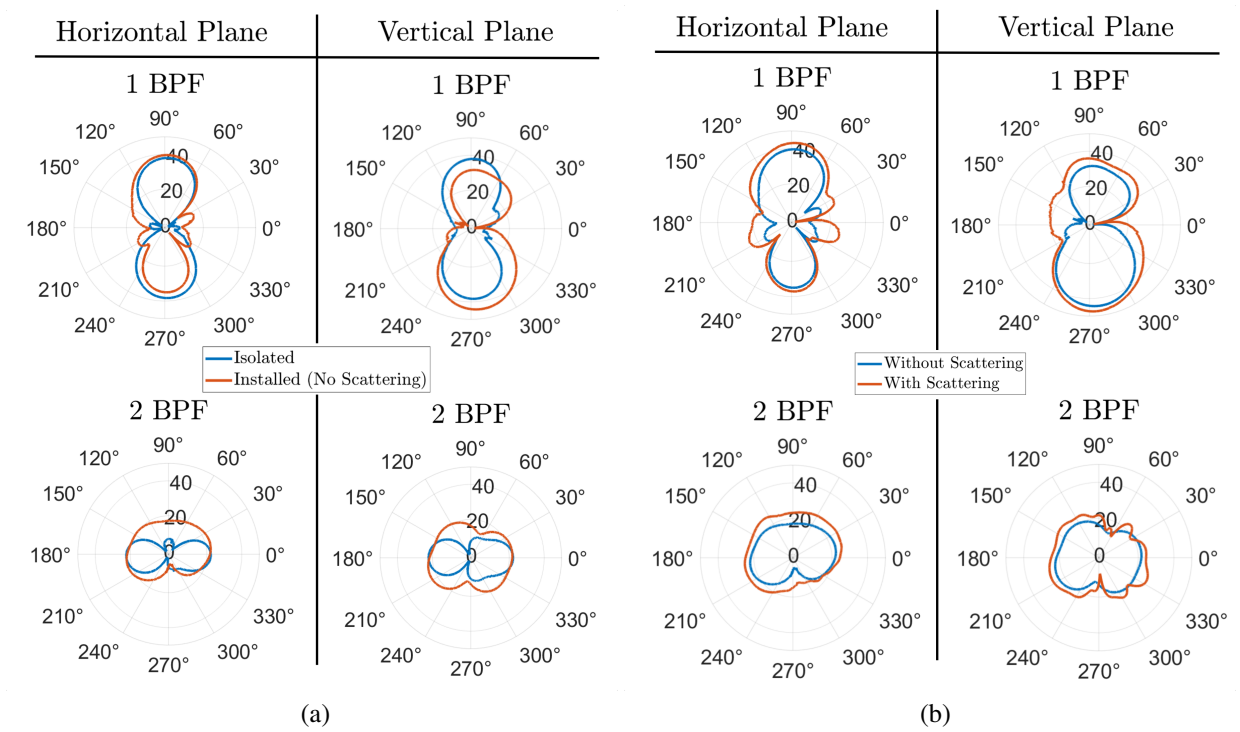

Fig. 8 (a) Directivity of XPROP-S propeller blade sound at $10D$ from free acoustic propagation with and without the aerodynamic presence of the wing. (b) Directivity of XPROP-S propeller blade sound at $10D$: comparing the installed blade sources in free field propagation and in the acoustic presence of the wing body.

F. Wing Noise

We can now compare the noise emitted by the propeller, subject to the aerodynamic installation effects, with the noise radiated by the equivalent dipoles generated from the unsteady pressure fluctuations on the wing itself. The pressure fluctuations on the region of the wing that is wetted by the propeller slipstream are predominantly induced by the impingement of the spinning blade wakes. It should however be noted that because we solve the compressible Navier-Stokes simulations, albeit with a low-order discretization scheme, we cannot exclude that the dipoles carried by the wing account not only for the wake interaction but also for the acoustic scattering of the propeller near-field emissions.

From the results shown in Figure 9, it is concluded that wing noise is a very important source of noise when considering a propeller-wing configuration such as this. In the horizontal plane, both the wing and the blade sources have approximately the same peak SPL however, the directivities are very distinct. As previously discussed, the propeller noise is primarily in the plane of the rotor; the wing noise, however, is dominant in the perpendicular direction. This follows what is expected considering the dominant orientation of the wing normal vectors along which the dipole elements radiate. In the vertical plane, the wing noise dominates in almost every direction often by more than 18 dB with a maximum difference of 20.0 dB at the 1^{st} BPF. The shape of the directivity is also indicative of the two surfaces of the wing (pressure side and suction side) generating noise with distinct lobes above and below the horizontal axis. The second BPF follows the same trends in the vertical plane and is less consistent in the horizontal plane but also generally follows the same directivity trends.

IV. Conclusions

The work reported in this paper permits drawing some conclusions about the relative importance of aerodynamic and aeroacoustic installation effects in tractor DEP configurations. The key questions were about the relative importance of the propeller and wing as equivalent sources, and how the presence of the wing is affecting the propeller blade forces and acoustic scattering.

The impact of the wing on the steady aerodynamics of the propeller was found to be minimal, as the large distance

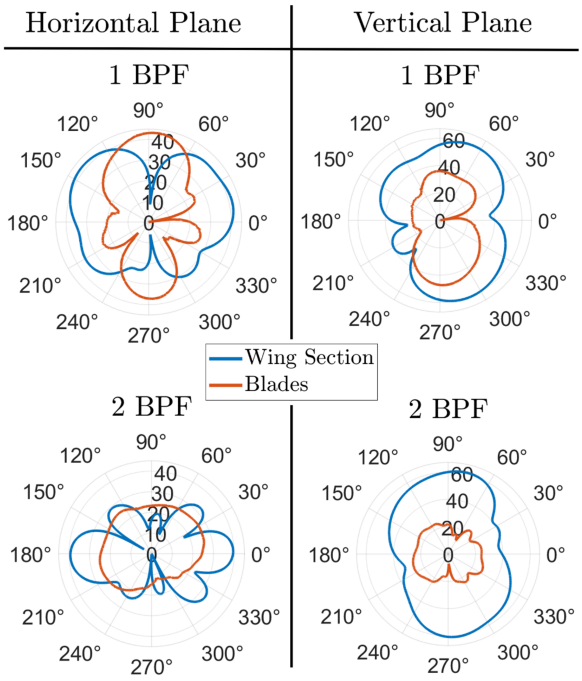

Fig. 9 The directivity of the blade noise and wing noise, both including scattering effects from the wing.

between the rotor plane and the leading edge of the wing resulted in a slight increase in thrust by 3.5% of the propeller blades being observed. In contrast, the presence of the wing caused a significant increase in the first thrust BLHs, well above the variations that could be attributed to the simulation uncertainty.

This significant increase in the BLHs is somehow unexpected if we start from the assumption that the dominant interaction would be the distortion of the flow field traversed by the blades that is caused by the deflection of the streamlines as they approach the leading edge. This potential effect is indeed known to be localized in a region that scales roughly with the radius of curvature of the leading edge [29], while the propeller is placed much further upstream. We conjecture that the strengthened BLHs are actually mostly associated with the upwash mean velocity induced by the lifting wing, inducing an off-axis incoming inflow on the propeller plane. This potential interaction, apparent from the trajectory of the tip vortex path, extends indeed at much larger distances. It would be difficult to avoid unless the supporting pylon is considerably lengthened, making it an impractical solution. In addition, the associated noise generation would depend on the angle of attack of the aircraft.

The result of this aerodynamic installation is a change in directivity at the two first BPFHs with the largest change at the first BPF being a 6.94 dB increases below the wing and a large increase in the plane of rotation at the second BPF. The radiation of the second BPF is however much weaker, with peak emissions about 20 dB below those of the first BPF.

The acoustic installation had a slightly lower effect at both harmonics, not changing the overall shape by much but increasing the noise in almost every direction by an average of 3.12 dB in the lobes. The scattering of the leading edge does, however, cause an increase of up to 20 dB in the axial direction where there was previously negligible noise.

But for the downward radiation directions, the most significant source of noise appears to be the wing subjected to the incoming wakes of the propeller blades, and its associated equivalent dipoles. In the vertical plane, the sound from the wing dominates the propeller noise by more than 20 dB in some directions. It turns out that despite the Doppler amplification that applies to the propeller blade, the acoustic non-compactness of the wing makes it a more efficient acoustic source. The predominance of the wing dipolar field is even more marked for the second BPF, with acoustic levels similar to those of the first BPF, whereas the propeller noise is much reduced for this second BPF.

In the future, determining the dependence of higher harmonics on numerical refinement will be of interest. The hybrid approach presented in this work will also permit investigating the effects of different wing shapes, blade-leading-edge distances, and multi-propeller configurations to understand how different variables affect the overall noise, discriminating between potential and viscous, and the aerodynamic and acoustic installation effects.

Acknowledgements

The authors thank the Technische Universiteit Delft (Netherlands) for providing the X-PROP-S CAD model used in the simulations. The kind support of Dr. Korcan Kucukcoskun and Dr. Sophie Le Bras, regarding the CFD and numerical acoustic simulations, is gratefully acknowledged as well.

This project has received funding from the European Union's Horizon 2020 research and innovation programme under grant agreement No 860103.

References

[1] Grandl, G., Salib, J., and Kirsch, J., "The Economics of Vertical Mobility: A guide for investors, players, and lawmakers to succeed in urban air mobility," *Porsche Consulting*, 2021.

[2] Borer, N. K., Patterson, M. D., Viken, J. K., Moore, M. D., Bevirt, J., Stoll, A. M., and Gibson, A. R., *Design and Performance of the NASA SCEPTOR Distributed Electric Propulsion Flight Demonstrator*, 2016. https://doi.org/10.2514/6.2016-3920.

[3] Hermetz, J., Ridel, M., and Doll, C., "Distributed electric propulsion for small business aircraft a concept-plane for key-technologies investigations." *ICAS 2016*, 2016.

[4] "EHang 216," *TransportUp webpage*, 2023. URL https://transportup.com/ehang-216/.

[5] "Airbus CityAirbus," *EVTOL News: Vertical Flight Society*, 2023. URL https://evtol.news/airbus-helicopters/.

[6] Stokkermans, T. C. A., Usai, D., Sinnige, T., and Veldhuis, L. L. M., "Aerodynamic Interaction Effects Between Propellers in Typical eVTOL Vehicle Configurations," *Journal of Aircraft*, Vol. 58, No. 4, 2021, pp. 815–833. https://doi.org/10.2514/1.C035814.

[7] Johnson, W., Silva, C., and Solis, E., "Concept vehicles for VTOL air taxi operations," *AHS Technical Conference on Aeromechanics Design for Transformative Vertical Flight*, 2018.

[8] Christian, A. W., and Cabell, R., "Initial Investigation into the Psychoacoustic Properties of Small Unmanned Aerial System Noise," *23rd AIAA/CEAS Aeroacoustics Conference*, 2017. https://doi.org/https://doi.org/10.2514/6.2017-4051.

[9] Mulero-Pázmány, M., Jenni-Eiermann, S., Strebel, N., Sattler, T., Negro, J. J., and Tablado, Z., "Unmanned aircraft systems as a new source of disturbance for wildlife: A systematic review," *PLOS ONE*, Vol. 12, No. 6, 2017, pp. 1–14. https://doi.org/10.1371/journal.pone.0178448, URL https://doi.org/10.1371/journal.pone.0178448.

[10] Goldstein, M. E., "Aeroacoustics," *McGraw-Hill International Book Company*, 1976.

[11] Roger, M., and Moreau, S., "Tonal-Noise Assessment of Quadrotor-Type UAV Using Source-Mode Expansions," *Acoustics*, Vol. 2, No. 3, 2020, pp. 674–690. URL https://www.mdpi.com/2624-599X/2/3/36.

[12] Williams, J. E. F., and Hawkings, D. L., "Sound Generation by Turbulence and Surfaces in Arbitrary Motion," *Philosophical Transactions of the Royal Society of London. Series A, Mathematical and Physical Sciences*, Vol. 264, No. 1151, 1969, pp. 321–342. URL http://www.jstor.org/stable/73790.

[13] Torija, A. J., and Clark, C., "A Psychoacoustic Approach to Building Knowledge about Human Response to Noise of Unmanned Aerial Vehicles," *International Journal of Environmental Research and Public Health*, Vol. 18, No. 2, 2021. https://doi.org/10.3390/ijerph18020682.

[14] Roger, M., and Kucukcoskun, K., "Near-and-far field modeling of advanced tail-rotor noise using source-mode expansions," *Journal of Sound and Vibration*, Vol. 453, 2019, pp. 328–354. https://doi.org/https://doi.org/10.1016/j.jsv.2019.02.007, URL https://www.sciencedirect.com/science/article/pii/S0022460X19300926.

[15] Zawodny, N. S., Boyd, D. D., and Nark, D. M., *Aerodynamic and Acoustic Interactions Associated with Inboard Propeller-Wing Configurations*, 2021. https://doi.org/10.2514/6.2021-0714.

[16] de Vries, R., van Arnhem, N., Sinnige, T., Vos, R., and Veldhuis, L. L., "Aerodynamic interaction between propellers of a distributed-propulsion system in forward flight," *Aerospace Science and Technology*, Vol. 118, 2021, p. 107009. https://doi.org/https://doi.org/10.1016/j.ast.2021.107009, URL https://www.sciencedirect.com/science/article/pii/S1270963821005198.

[17] Duivenvoorden, R., Suard, N., Sinnige, T., and Veldhuis, L. L., *Experimental Investigation of Aerodynamic Interactions of a Wing with Deployed Fowler Flap under Influence of a Propeller Slipstream*, 2022. https://doi.org/10.2514/6.2022-3216, URL https://arc.aiaa.org/doi/abs/10.2514/6.2022-3216.

[18] Boermans, L., and Rutten, P., "Two-dimensional aerodynamic characteristics of airfoil NLF-MOD22 with fowler flap," *rep., Delft University of Technology, Delft*, 1995.

[19] Siemens Digital Industries Software, "Simcenter STAR-CCM+ User Guide v. 2021.1 (17.02 R8)," , Siemens 2021.

[20] Menter, "Two-equation eddy-viscosity turbulence models for engineering applications," *AIAA Journal*, Vol. 32, No. 8, 1994, pp. 1598–1605. https://doi.org/10.2514/3.12149.

[21] Zarri, A., Christophe, J., Moreau, S., and Schram, C., "Influence of Swept Blades on Low-Order Acoustic Prediction for Axial Fans," *Acoustics*, Vol. 2, No. 4, 2020, pp. 812–832. https://doi.org/10.3390/acoustics2040046, URL https://www.mdpi.com/2624-599X/2/4/46.

[22] Zarri, A., Dell'Erba, E., Munters, W., and Schram, C., "Aeroacoustic installation effects in multi-rotorcraft: Numerical investigations of a small-size drone model," *Aerospace Science and Technology*, Vol. 128, 2022, p. 107762. https://doi.org/https://doi.org/10.1016/j.ast.2022.107762.

[23] *Simcenter Nastran Acoustics User's Guide (version 2022.1)*, Siemens, 2022.

[24] Beriot, H., and Modave, A., "An automatic perfectly matched layer for acoustic finite element simulations in convex domains of general shape," *International Journal for Numerical Methods in Engineering*, Vol. 122, 2021, pp. 1239–1261. https://doi.org/10.1002/nme.6560.

[25] Roger, M., *Aeroacoustics of installed propellers*, No. 2019-02 in von Karman Institute Lecture Series, von Karman Institute for Fluid Dynamic, 2019.

[26] Tam, C. K., "Computational aeroacoustics: an overview of computational challenges and applications," *International Journal of Computational Fluid Dynamics*, Vol. 18, No. 6, 2004, pp. 547–567.

[27] Farassat, F., and Succi, G. P., "A review of propeller discrete frequency noise prediction technology with emphasis on two current methods for time domain calculations," *Journal of Sound and Vibration*, Vol. 71, No. 3, 1980, pp. 399–419.

[28] Schram, C., Bériot, H., Roger, M., Reese, H., and Carolus, T., "On the importance of near-field terms in the assessment of acoustic installation effects for ducted low-Mach number fans," *15th AIAA/CEAS Aeroacoustics Conference (30th AIAA Aeroacoustics Conference)*, 2009, p. 3334.

[29] Zamponi, R., Moreau, S., and Schram, C., "Rapid distortion theory of turbulent flow around a porous cylinder," *Journal of Fluid Mechanics*, Vol. 915, 2021, p. A27.